CrystEngComm

ARTICLE

Disclosing the Electronic Structure and Optical Properties of $Ag_4V_2O_7$ crystals: Experimental and Theoretical Insights

Received 18th May 2016,
Accepted 00th January 20xx

DOI: 10.1039/x0xx00000x

www.rsc.org/

R.C. de Oliveira[a], L. Gracia[b], M. Assis[a], M. Siu Li[c], J. Andres[b], L.S. Cavalcante[d]*, E. Longo[e]

This work combines experimental and computational techniques to exploit the best of both methodologies and thus provide a tool for understanding the geometry, cluster coordination, electronic structure, and optical properties of $Ag_4V_2O_7$ crystals. This tool has been developed to create structural models and enable a much more complete and rapid refinement of 3D (Third Dimension) structures from limited data, aiding the determination of structure-property relationships and providing critical input for materials simulations. $Ag_4V_2O_7$ crystals were synthesized by a simple precipitation method from aqueous solution at 30 °C for 10 min. The obtained crystals were characterized by X-ray diffraction (XRD) and Rietveld refinement, and micro-Raman spectroscopy. The crystal morphology was determined by field emission scanning electron microscopy (FESEM), and the optical properties were investigated by ultraviolet-visible (UV-vis) diffuse reflectance spectroscopy and photoluminescence (PL) measurements. The geometric and electronic structures of $Ag_4V_2O_7$ crystals were investigated by first-principles quantum-mechanical calculations based on the density functional theory. The theoretical results meet the experimental data to confirm that $Ag_4V_2O_7$ crystals have an orthorhombic structure, and that the building blocks of the lattice comprise two types of V clusters, $[VO_4]$ and $[VO_5]$, and two types of Ag clusters, $[AgO_5]$ and $[AgO_6]$. This type of fundamental studies, which combine multiple experimental methods and first-principles calculations, have been proved valuable to obtain a basic understanding of the local structure, bonding, electronic, and optical properties of $Ag_4V_2O_7$ crystals.

1. Introduction

In recent years, silver vanadates ($AgVO_3$, $Ag_2V_4O_{11}$, Ag_3VO_4, $Ag_4V_2O_7$, etc.) have attracted increasing attention due to their widespread potential applications resulting from their special optical, electronic, and chemical properties[1-18]. The excellent properties of silver vanadates can be attributed to the flexibility of their geometric structure, in which Ag and V ions can adopt different local coordinations, as well as the electronic properties associated to the hybridization of the valence bands of the V 3*d*, O 2*p*, and Ag 4*d* orbitals, yielding a narrow band gap and highly dispersed valence bands[19-21].

Among the reported silver vanadates, silver pyrovanadate ($Ag_4V_2O_7$) has drawn extensive interest in the field of photocatalysis[6,7,10]. Various techniques, such as mechanochemical reactions[22], oxide mixture or solid-state reaction[2], precipitation with calcination at long times[2], and molten metal fluxes[23] have been reported. However, these methods require high temperatures, long processing times, and sophisticated equipment with high maintenance costs. In addition, the final product is obtained with some deleterious phases, such as V_2O_5, amorphous $AgVO_3$, Ag_3VO_4, and Ag_2O, with inhomogeneous sizes and shapes. To avoid these drawbacks, several synthetic routes have recently been developed and employed in the preparation of $Ag_4V_2O_7$ micro and nanocrystals[10,24], and pure $Ag_4V_2O_7$ crystals have been obtained through several wet chemistry-based techniques, such as conventional and surfactant-assisted hydrothermal syntheses[5,7,9,25] or microemulsions[26]. These methods circumvent the problems encountered in earlier synthetic methods and facilitate the synthesis of single phase crystals with homogeneous sizes and shapes. In particular, our lab has successfully achieved the preparation of various complex ternary metal oxides, including α-Ag_2WO_4[27] and β-Ag_2WO_4[28], using facile and readily scalable techniques in environmentally friendly solvents (water) at low processing temperatures.

To the best of our knowledge, the geometric and electronic structures of $Ag_4V_2O_7$ crystals have not been investigated

[a] INCTMN-UFSCar, Universidade Federal de São Carlos, P.O. Box 676, 13565–905, São Carlos, SP, Brazil.
[b] Departament de Química Física i Analítica, Universitat Jaume I, 12071, Castelló de la Plana, Spain.
[c] IFSC-Universidade de São Paulo, P.O. Box 369, 13560-970 São Carlos, São Paulo, Brazil
[d] PPGQ-Universidade Estadual do Piauí, Rua João Cabral, 2231, P.O. Box 381, 64002–150, Teresina, PI, Brazil.
[e] INCTMN-UNESP, Universidade Estadual Paulista, P.O. Box 355, 14801–907 Araraquara, SP, Brazil
*laeciosc@gmail.com;

†Electronic Supplementary Information (ESI) available: [details of any supplementary information available should be included here]. See DOI: 10.1039/x0xx00000x

either theoretically or experimentally. This encouraged us to investigate the geometry, cluster coordination, and electronic structure of $Ag_4V_2O_7$ microcrystals. Five years ago, our research groups initiated a major experimental and theoretical collaboration to elucidate the structure, chemical bonding, electronic, and optical properties of numerous ternary metal oxide photocatalysts, bactericides, sensors, photoluminescent complexes, etc., such as α-Ag_2WO_4[27,29-31], β-Ag_2WO_4[28,32], β-Ag_2MoO_4[33], and Ag_3PO_4[34, 35]. These studies have made significant advances in the formal understanding of the properties and application of these compounds at a qualitative or semiquantitative level, by combining experimental data and first-principles calculations.

Here, we report for the first time the synthesis of $Ag_4V_2O_7$ microcrystals by a simple precipitation method at low temperature. The synthesized $Ag_4V_2O_7$ crystals were characterized by X-ray diffraction (XRD) and Rietveld refinement, Raman spectroscopy, field emission scanning electron microscopy (FESEM), ultraviolet-visible (UV-vis) diffuse reflectance spectroscopy, and photoluminescence (PL) measurements. First-principles quantum-mechanical calculations using density functional theory (DFT) were carried out in order to correlate the results of XRD, Raman spectroscopy, FESEM, and the PL measurements for$Ag_4V_2O_7$. There is a need to link the length and complexity scales between the levels of theory used in calculations and the variable space in which experiments take place; the present work can thus be considered an attempt to bridge this gap.

2. Method Experimental and Theoretical

2.1. Experimental details

The precursors utilized in this synthesis were silver nitrate, $AgNO_3$ (99,0% purity, Synth) and ammonium monovanadate, NH_4VO_3 (99% purity, Aldrich). Initially, 1×10^{-3} mol de NH_4VO_3 were dissolved in 60 mL distilled water at 30°C, under magnetic stirring for 15 minutes. Then, 1×10^{-3} mol of $AgNO_3$ were dissolved in 15 mL distilled water, under magnetic stirring for 15 minutes, to this solution was added a few drops of ammonium hydroxide (NH_4OH) (30% in NH_3, Synth) until the solution becomes clear. Both solutions were quickly mixed, promoting the instantaneous formation of solid $Ag_4V_2O_7$ precipitates (orange coloration). To accompany the change of morphologies, the PM was performed at 30 ºC for 10 min. The precipitate was centrifuged, washed with distilled water several times, and dried in a conventional furnace at 60 ºC for some hours.

2.2. Characterization

X-ray diffraction using a Rigaku-DMax/2500PC (Japan) with Cu Kα radiation (λ = 1.5406 Å) in the 2θ range from 10° to 80° with a scanning rate of 0.02°/min. Micro-Raman spectroscopy was carried out using an T64000 spectrometer (Horiba obin-Yvon, Japan) coupled to a CCD Synapse detector and an argon-ion laser, operating at 514 nm with maximum power of 7 mW. The spectra were measured in the range from 100 cm^{-1} to 1100 cm^{-1}. UV-vis spectra were obtained in a Varian spectrophotometer model Cary 5G (USA) in diffuse reflection mode. The morphologies were investigated with a field emission scanning electron microscopy (FE-SEM) Supra 35-VP Carl Zeiss (Germany) operated in 15 KV. The PL measurements were performed with a Monospec 27 monochromator Thermal Jarrel Ash (USA) coupled to a R446 photomultiplier Hamamatsu Photonics (Japan). A krypton ion laser Coherent Innova 90 K (USA) (λ = 350 nm) was used as excitation source, keeping its maximum output power at 500 mW. All experiments measurements were performed at room temperature.

2.3. Theoretical Calculations

Calculations on the periodic $Ag_4V_2O_7$ structure were performed with the CRYSTAL14 sofware package[36]. Tungsten was described by a large-core ECP, derived by Hay and Wadt, and modified by Cora *et al*.[37]. Silver and oxygen centers were described using HAYWSC-311d31G and O (6-31d1G) basis sets, respectively, which were taken from the Crystal web site[38]. A Range-separated hybrid functional, the screened-Coulomb HSE06 was used in order to give the accurate band gaps for the computed structures. The diagonalization of the Fock matrix was performed at adequate *k*-points grids in the reciprocal space. The thresholds controlling the accuracy of the calculation of the Coulomb and exchange integrals were set to10^{-8} and 10^{-14}, and the percent of Fock/Kohn-Sham matrices mixing was set to 40 (IPMIX keyword)[36]. The empirical correction scheme to energy that considers the long-range dispersion contributions proposed by Grimme[39] and implemented by Bucko et al.[40] for periodic systems was used. In the relaxed configuration, the forces on the atoms are less than 0.0001 hartree/bohr = 0.005 eV/Å, and deviations of the stress tensor from a diagonal hydrostatic form are less than 0.1 GPa. The band structure and the density of states (DOS) projected on atoms and orbitals of bulk $Ag_4V_2O_7$ was constructed along the appropriate high-symmetry directions of the corresponding irreducible Brillouin zone. The vibrational-frequencies calculation in CRYSTAL is performed at the Γ-point within the harmonic approximation, and the dynamic matrix is computed by the numerical evaluation of the first derivative of analytical atomic gradients.

First-principles total-energy calculations on the periodic $Ag_4V_2O_7$ structure were performed within the density functional theory (DFT) along with projector augmented wave (PAW) potentials implemented in the VASP program[41]. The Kohn-Sham equations were solved using the screened hybrid functional proposed by Heyd, Scuseria, and Ernzerhof (HSE)[42], in which a percentage of exact nonlocal Fock exchange was added to the Perdew, Purke, and Ernzerhof functional (25%), with a screening of 0.2 $Bohr^{-1}$ applied to the partition of the Coulomb potential into long-range and short-range terms. The plane-wave expansion was truncated at cut-off energy of 400 eV and the Brillouin zones were sampled through Monkhorst-Pack special *k*-points grids to ensure geometrical and energetic convergence. Conjugate gradient algorithms were used for

unit-cell relaxations and atomic positions, until the residual forces and stress in the equilibrium geometry were of the order of 0.005 eV $Å^{-1}$ and 0.01 GPa, respectively. The band structure and the density of states (DOS) projected on the atoms and orbitals of bulk $Ag_4V_2O_7$ were constructed along the appropriate high-symmetry directions of the corresponding irreducible Brillouin zone. Vibrational-frequency calculations were performed at the Γ-point within the harmonic approximation, and the dynamic matrix was computed by a numerical evaluation of the first derivative of the analytical atomic gradients.

3. Results and discussion

3.1. XRD pattern and Rietveld refinement analysis

Figures 1(a) and 1(b) show the XRD pattern and Rietveld refinement plot of the $Ag_4V_2O_7$ microcrystals, respectively.

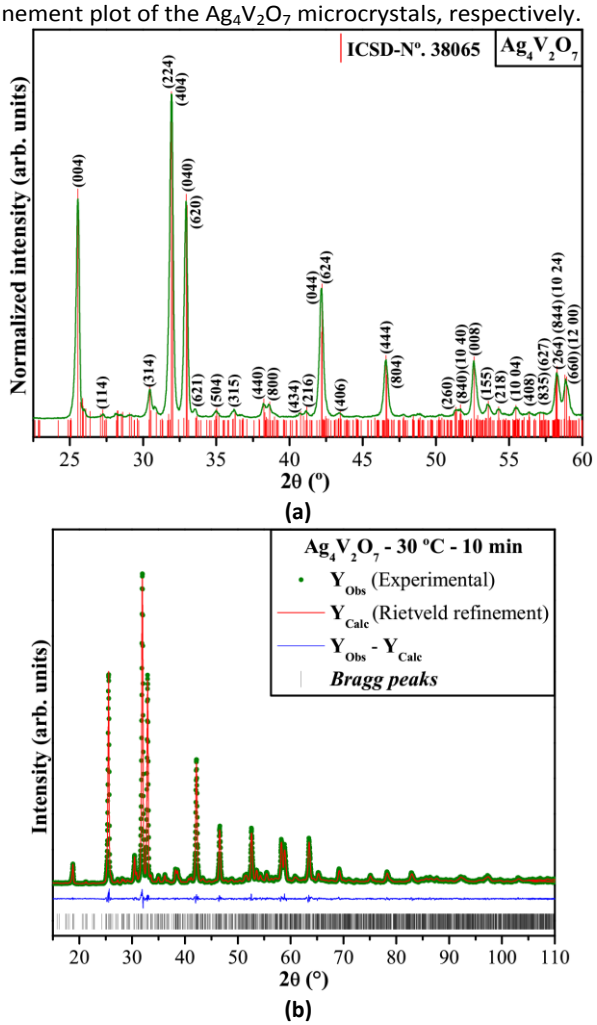

Fig. 1: (a) XRD patterns of 3D hexagons-like $Ag_4V_2O_7$ microcrystals obtained at 30 ºC for 10 min and **(b)** Rietveld refinement plots 3D hexagons-like $Ag_4V_2O_7$ microcrystals, respectively. The vertical lines in black colour indicate the position and relative intensity of the Inorganic Crystal Structure Database (ICSD) card N°. 38065 for $Ag_4V_2O_7$ phase, respectively.

$Ag_4V_2O_7$ was first characterized by Masse et al. [23] and Fig. 1(a) shows the XRD pattern corresponding to the orthorhombic structure, in agreement with the corresponding Inorganic Crystal Structure Database (ICSD) card N°. 38065 for the pure $Ag_4V_2O_7$ phase [23]. According to the literature [23], pure $Ag_4V_2O_7$ microcrystals present a space group (*Pbca*),a point-group symmetry (D_{2h}^{15}), and sixteen molecular formula units per unit cell (Z = 16). In order to confirm this result, a structural refinement by means of the Rietveld method [43], based on the construction of diffraction patterns calculated according to a structural model [44], was performed using the general structure analysis (GSAS) program [45].

The calculated patterns were adjusted to fit the observed patterns and thus provide the structural parameters of the material and the diffraction profile. In this work, the Rietveld method was applied to adjust the atomic positions, lattice parameters, and unit cell volume. Figure 1(b) shows that the structural refinement results are mostly consistent with the ICSD No. 38065 reported by Masse et al.[23]. However, the low-angle region, where the most intense peaks are located, reveals a major difference related to narrow peaks and high intensities in the pattern.

The quality of a structural refinement is generally examined using R-values (R_{wp}, R_{Bragg}, R_p, χ^2, and S).These values were determined for our crystals and found to be consistent with an orthorhombic structure. However, the experimentally observed XRD patterns and theoretically calculated data display small differences near zero on the intensity scale, as illustrated by the line Y_{Obs}–Y_{Calc}. More details regarding the Rietveld refinement results are displayed in Table S1. The Rietveld refinement plot for the $Ag_4V_2O_7$ microcrystals is shown in Fig. 1(b).

3.2. Unit cell representation and symmetry, geometry, and coordination of the clusters in $Ag_4V_2O_7$ crystals

Figures 2(a) and 2(b) show a schematic representation of the orthorhombic $Ag_4V_2O_7$ unit cell in which different clusters, i.e. the local coordination of V and Ag atoms, are depicted. The symmetry, geometry, and coordination data for each cluster, as well as the lattice parameters and atomic positions calculated by geometry optimization, are listed, while those obtained from the Rietveld refinement data are presented in Table S1.

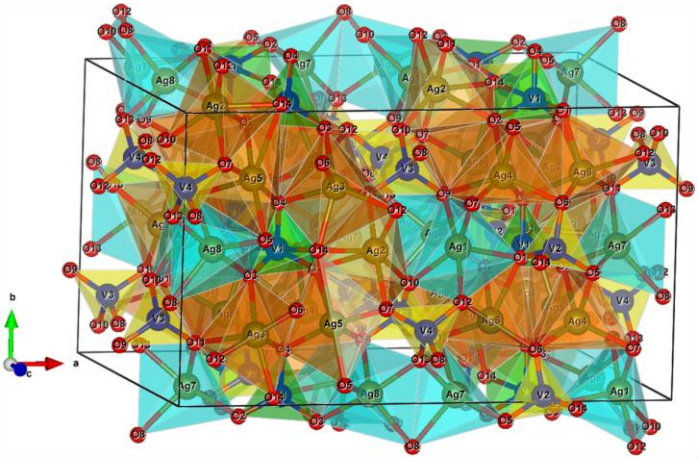

(a)

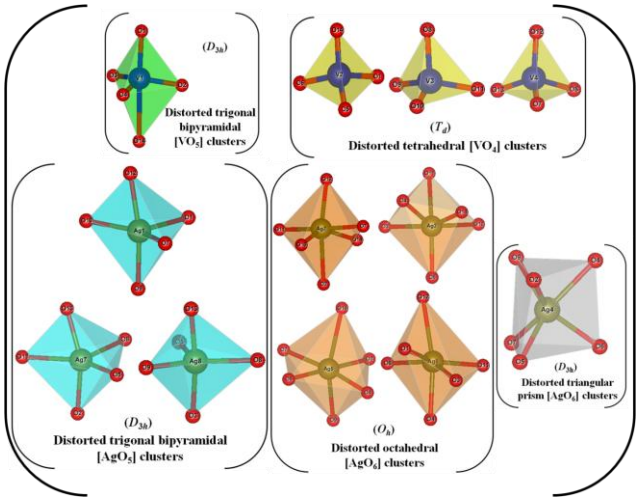

(b)

Fig. 2: Schematic representation of the (a) orthorhombic unit cells corresponding to pure $Ag_4V_2O_7$ crystals and **(b)** their clusters, respectively.

The unit cell shown in Fig. 2(a) and Fig. 2(b) was modeled through the Visualization System for Electronic and Structural Analysis (VESTA) program (version 3.3.2 for Windows 7-64-bit)[46, 47]. Analysis of the results indicated that two types of clusters are the main building blocks of the structure for both V and Ag atoms: $[VO_4]$ and $[VO_5]$, in which V atoms are coordinated to four and five O atoms, respectively, and $[AgO_5]$ and $[AgO_6]$, in which Ag atoms are linked to five and six O atoms, respectively. The different types of local coordination for the Ag and V atoms, together with the Ag–O and V–O bond lengths corresponding to the minima, *D*min, and maxima, *D*max, are listed in Fig. 2(a). Analysis of the results revealed that $[VO_4]$ and $[VO_5]$ clusters are distorted tetrahedral and distorted trigonal bipyramidal polyhedral clusters, respectively. V1 and V4 (Fig. 2(a)) form distorted trigonal bypiramidal $[VO_5]$ clusters, while V2 and V3 form tetrahedral $[VO_4]$ clusters. Atoms Ag1 and Ag7, as well as Ag8,are coordinated to five O atoms, forming distorted square-based pyramidal and distorted trigonal $[AgO_5]$ clusters, respectively; while Ag2, Ag3, Ag5, and Ag6 are bonded to six O atoms, which form distorted octahedral $[AgO_6]$ clusters;andAg4 is at the center of a distorted triangular prism $[AgO_6]$.

The lattice parameters, unit-cell volume, and internal atomic coordinates for $Ag_4V_2O_7$from the Rietveld refinement and DFT calculations are reported in Table S1 (a) and (b) (SI), respectively. Analysis and comparison of both theoretical and experimental results show variations in the atomic positions of O atoms, associated with the fact that these atoms do not occupy fixed positions in the orthorhombic structure. Large variations in the position of O atoms in the lattice are also found in the structure. These findings explain why assignment of the atomic positions of O atoms is difficult, since subtle atomic rearrangements occur.

In order to interpret these data, we presume that these disagreements in the atomic positions of O atoms are attributed to the nature of the starting sample (polycrystalline powder or single crystal). Although single-crystal data are essential for the refinement of crystal-structure models, we believe that the formation of different distortions in the cluster coordination, $[AgO_y]$ (y = 5 and 6) and $[VO_z]$ (z = 4 and 5), can lead to the formation of different types of distortions in the Ag–O and/or V–O bonds, as well as the O–Ag–O and/or O–V–O bond angles. This is due to the fact that cluster rotation influences the Ag–O and V–O bond lengths, as well as the Ag–O–Ag and V–O–V bond angles, due to the shift of the oxygen ions from the edge of the ideal structures. Therefore, the differences in both Ag–O and V–O bond lengths and O–Ag–O and O–V–O bond angles result in intrinsic structural order–disorder in this type of lattice, and $Ag_4V_2O_7$ crystals thus present different levels of distortion in their crystalline lattice due to the variety of coordination polyhedra. Subsequently, the positions of O, V, and Ag atoms are variable. A similar phenomenon has been previously reported for the α-Ag_2WO_4[48] and β-Ag_2WO_4 phases[28]. XRD experiments provide only average structures.

A better understanding of the properties of this material requires more detailed information on local structures and cell parameters. In other words, if there is partial order in the distribution of Ag and V atoms, crystal cells observed at the local level should be different from those determined by XRD measurements. Raman spectroscopy probes the full vibrational spectrum of interest since it is sensitive to short-range structural order, i.e., the local coordination at both Ag and V centers.

3.3. Micro-Raman spectroscopy analysis

Raman spectroscopy can be employed as a probe to investigate the degree of structural order–disorder in materials at short-range; in our case, the local coordination of both Ag and V atoms associated to different clusters, $[AgO_y]$ (y = 5 and 6) and $[VO_z]$ (z = 4 and 5), as the building blocks of $Ag_4V_2O_7$ crystals. To the best of our knowledge, the Raman characteristics of $Ag_4V_2O_7$ have not been previously reported, either theoretically or experimentally. Consequently, we extended our systematic structural investigation toward Raman spectroscopy and the theoretical analysis of the vibrational modes of $Ag_4V_2O_7$.The micro-Raman spectrum of $Ag_4V_2O_7$ microcrystals is shown in Fig. 3.

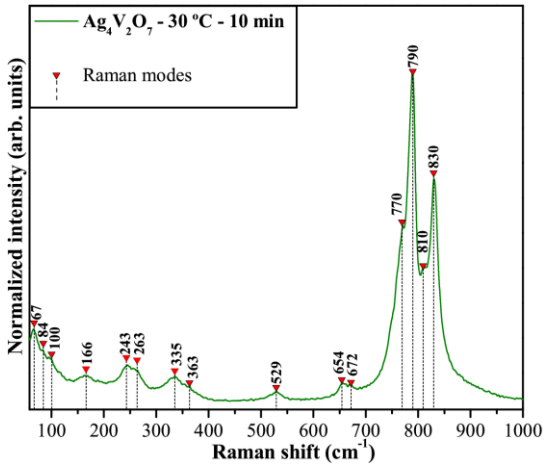

Fig. 3: Micro-Raman spectra of 3D hexagons-like $Ag_4V_2O_7$ microcrystals and comparison between the relative positions of the theoretical and experimental Raman-active modes, respectively.

The micro-Raman spectrum revealed the presence of only fifteen Raman-active vibrational modes (A_g, B_{1g}, B_{2g},and B_{3g}). It

is notable that the Raman spectrum of the synthesized crystals exhibits broad vibrational modes, indicating short-range structural disorder. This characteristic can be related to very rapid kinetics under the synthetic conditions and to intrinsic structural disorder in the lattice, as demonstrated by the Rietveld refinement and first-principles calculations.

Therefore, A_g, and B_g are Raman-active modes, and A_u, B_{1u}, B_{2u} and B_{3u} are active vibrational modes in the infrared spectrum. The A and B modes are nondegenerate; subscripts "$_g$" and "$_u$" indicate the parity under inversion in centrosymmetric $Ag_4V_2O_7$ crystals.

Analysis of the micro-Raman spectrum presented in Fig.3 revealed that the strongest Raman-active modes appear above770 cm^{-1} with symmetry B_{2g}, dominated by a Raman-active mode at 790 cm^{-1} related to the asymmetric stretching of the distorted trigonal bipyramidal [VO_5] clusters with character B_{1g} or B_{3g}. Other two B_{2g} Raman-active modes at 810 and 830 cm^{-1} are prominent, derived from the symmetric-stretching vibration of the distorted tetrahedral [VO_4] clusters.

According to group theory, crystals with orthorhombic structure, space group (*Pbca*), point-group symmetry (D_{2h}^{15}), and eight molecules per unit cell (Z = 8) exhibit 312 vibrational modes in the center of the Brillouin zone ($\vec{k} = 0$), as given by the equation [49]: $\Gamma_{\text{Raman+Infrared(Crystal Primitive)}} = \{(39A_g) + (39B_{1g}) + (39B_{2g}) + (39B_{3g}) + [39A_u] + [39B_{1u}] + [39B_{2u}] + [39B_{3u}]\}$. However, our 3D hexagon-like $Ag_4V_2O_7$ microcrystals have sixteen molecules per unit cell (Z = 16) and display 624 vibrational modes according to the following equation: $\Gamma_{\text{Raman+Infrared (Crystal Primitive)}} = \{(78A_g) + (78B_{1g}) + (78B_{2g}) + (78B_{3g}) + [78A_u] + [78B_{1u}] + [78B_{2u}] + [78B_{3u}]\}$.

The 312 theoretical Raman-active modes are shown in Table S2 (SI) and can be organized into two different groups. The first group is composed of modes in the frequency range of 13 to 508 cm^{-1} and is related to lattice phonons and the motion of distorted trigonal bipyramidal [AgO_5] clusters and distorted octahedral/triangular prism [AgO_6] clusters. These modes are basically associated to symmetric and/or asymmetric bending modes of the distorted tetrahedral [VO_4] clusters and distorted trigonal bipyramidal [VO_5] clusters. In the second group, at high frequencies and separated by a phonon gap of nearly 173 cm^{-1},are the modes corresponding to symmetric and/or asymmetric stretching of the distorted trigonal bipyramidal [VO_5] and distorted tetrahedral [VO_4] clusters.

A comparison of the experimental Raman active modes with the closest theoretically calculated ones is presented in Table S3.

A good agreement between the experimental and calculated Raman-active modes is observed, and these results allow us to confirm the 3D hexagon-like structure of the $Ag_4V_2O_7$ microcrystals obtained in this work.

FE-SEM images of the microcrystals are depicted in Fig. 4(a–c). Fig. 4(a) shows a large quantity of small $Ag_4V_2O_7$ microcrystals with a well-defined 3D hexagon-like morphology. Moreover, some of these hexagons have surface defects and are formed by small nanocrystals through a self-assembly process due to environment during the synthetic process. The microcrystals have an average size of approximately 2.7 µm width with a thickness of about 1 µm, and are formed through the aggregation of several nanocrystals and plates with an average size of approximately 375 nm, as can be seen in Fig. S2(a–d)(SI). These microcrystals have only 8 faces in the first few minutes of the reaction; however, after 10 min of the reaction at 30 °C, fast growth occurs to afford 3D hexagon-like $Ag_4V_2O_7$ microcrystals with 14 faces, as shown in Fig. S2(e) (SI). In Fig. 4(b), a series of $Ag_4V_2O_7$ microcrystals with a more defined shape can be observed due to thermodynamic processes and the chemical synthesis method employed. We also note that these crystals display a very regular shape and size, as is evident from Fig. 4(c) and the computationally simulated crystal shape shown in the inset.

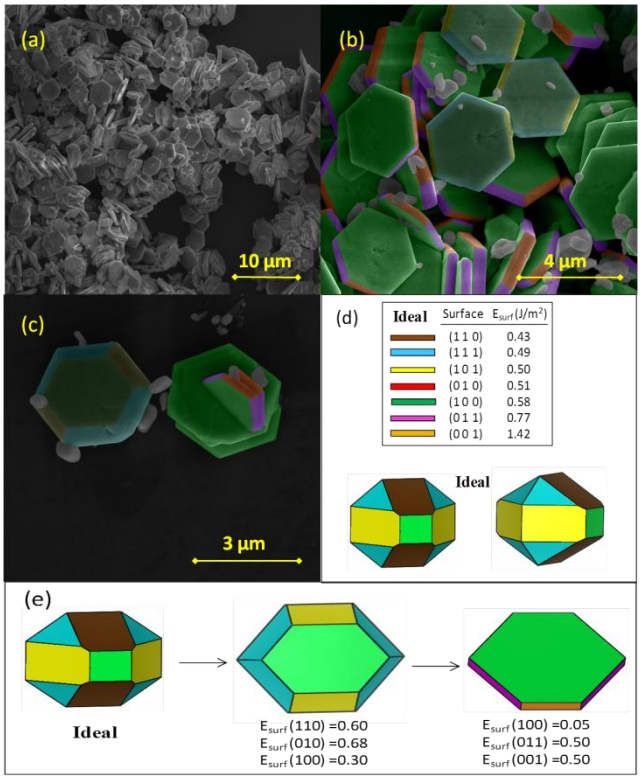

Fig. 4: FE-SEM images for 3D hexagons-like $Ag_4V_2O_7$ microcrystals: **(a)** low magnification, **(b)** intermediate magnification and **(c)** high magnification, **(d)** Crystal shape simulated computationally and their optimized surface energies (J/m^2) and **(e)** Crystal shape theoretical for $Ag_4V_2O_7$ microcrystals using BPE level, respectively.

Using a specific methodology, which has been applied to study morphologies of various metal oxides such as SnO_2 [50], $PbMoO_4$ [51], and $CaWO_4$ [52], we developed a combination of experimental studies with first-principles calculations to deeper investigate electronic, structural, and energetic properties controlling the morphology and related transformation mechanisms of various metals and metal oxides such as Ag, anatase TiO_2, $BaZrO_3$, and α-Ag_2WO_4 [53] as well as Co_3O_4, Fe_2O_3, and In_2O_3 [54]. These cited papers contain a description of the method for the calculation of the surface energies, which were used to characterize the corresponding surface morphologies using Wulff constructions.

The (100), (010), (001), (110), (101), (011), and (111) surfaces of the orthorhombic $Ag_4V_2O_7$ system were modeled by unreconstructed (truncated bulk) slab models using the calculated equilibrium geometry (a = 18.752 Å, b = 11.090 Å, c = 13.504 Å) and introducing a vacuum spacing of 15 Å in the z-direction so that the surfaces do not interact with each other. After the corresponding convergence test on the system, slab models containing 8 molecular units were selected, with areas of 149.8 $Å^2$, 153.2 $Å^2$, 208.0 $Å^2$, 294.2 $Å^2$, 256.4 $Å^2$, 327.7 $Å^2$,and 360.3 $Å^2$, for the (100), (010), (001), (110), (101), (011), and (111) surfaces, respectively. Analysis of the theoretical results indicates that the most stable surfaces are the (110), (111), and (101) facets, which can form an ideal morphology (shown in Fig. 4(d)).

When the relative stability of the facets changes (increases or decreases), more than one facet type appears in the resulting morphology, resulting in morphology variations. A3D hexagon-like $Ag_4V_2O_7$ morphology with 14 faces is obtained if the surface energies of (110) and (010) increase to 0.60 and 0.68 J/m^2, respectively, and the surface energy of (100) decreases to 0.30 J/m^2 (see Fig. 4(e)). However, a morphology having only 8 faces is produced when the surface energy of (100) decreases to 0.05 J/m^2 and that of (011) and (001) equals 0.5 J/m^2. Thus, variations in the ratio between the values of the surface energy affect the related morphologies, which can be used to obtain correlations with the experimental results.

Figs. 5(a,b) show the UV–vis diffuse reflectance spectra and calculated electronic band structure/density of states (DOS) of 3D hexagons-like $Ag_4V_2O_7$ crystals, respectively.

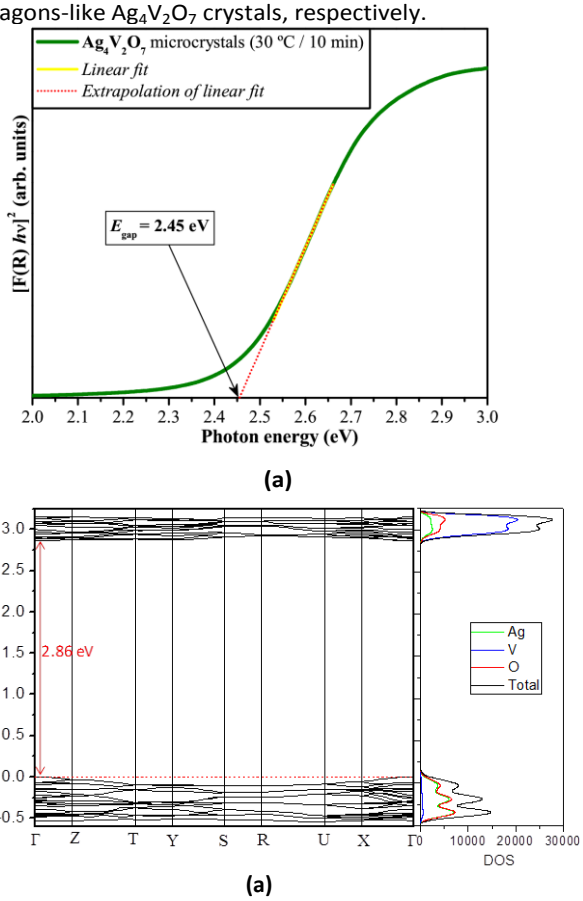

Fig. 5: **(a)** UV-Vis spectrum and **(b)** band structure/DOS for 3D hexagons-like $Ag_4V_2O_7$ microcrystals, respectively.

As seen in Fig. 5(a), an E_{gap} value of 2.45 eV was obtained for our 3D hexagon-like $Ag_4V_2O_7$ microcrystals, as calculated by extrapolating the linear portion of the UV-vis curve and Fig. 5(c) In principle, we believe that this behavior is related to presence of intermediary energy levels between the valence band (VB) and the conduction band (CB), since the exponential optical absorption edge and E_{gap} are controlled by the degree of structural order–disorder in the lattice. Calculations yield a direct band gap value of 2.86 eV from Γ to the Γ points in the Brillouin zone and, for a simplified description, this difference can be mainly attributed to the distortions of both tetrahedral/trigonal bipyramidal [VO_z] (z = 4 and 5) clusters and trigonal bipyramidal/octahedral [AgO_y] (y= 6 and 5) clusters at short- and medium-range, and is present in Fig 5 (b).

At this point, it is important to note that determination of the structural order–disorder in a crystalline solid plays a crucial role in the understanding of the relation between its physical properties and its electronic structure, and advanced methodologies allow nowadays for the precise control of the composition and properties of nanomaterials[55,56]. For a given material, structural disorder can present useful properties, such as ferroelectricity, piezoelectricity, and nonlinear optical behavior[57-60]. Therefore, it is important to create disorder in order to obtain new materials with unique physical properties that would be otherwise inaccessible in well-ordered crystal structures[61]. In this context, PL properties are environment-sensitive and significantly affected by the structural order–disorder degree that accompany changes in crystal size and morphology during the synthetic process.

The PL spectrum at room temperature of $Ag_4V_2O_7$ microcrystals is shown in Fig. 6.

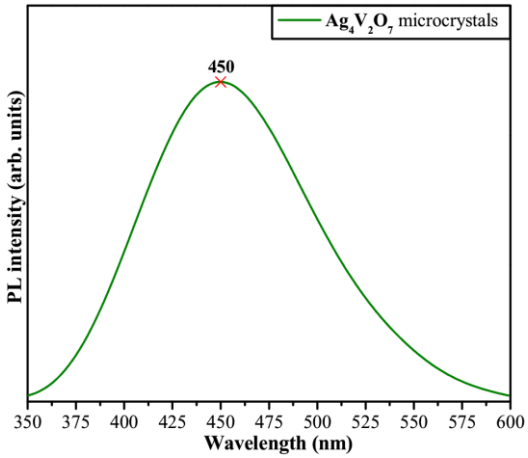

Fig. 6: PL emission spectrum for 3D hexagons-like $Ag_4V_2O_7$ microcrystals,

The PL spectrum exhibits a typical broad band profile, which can be associated with multiphonon or multilevel processes, i.e., a solid system where relaxation occurs by several pathways that involve the participation of numerous energy states within the band gap. The PL spectrum covers a broad range of wavelengths, from 355 to 600 nm, centered at

450 nm in the blue region of the visible spectra for the 3D hexagon-like $Ag_4V_2O_7$ microcrystals (see Fig. 6).

The photoluminescence emission of vanadate-based compounds has been associated with charge transfer transitions from the oxygen ligands O^{2-} to the central vanadium ions V^{5+} in $[VO_4]$ tetrahedra, as well as complex cluster vacancies and/or modified lattices[62,63]. However, all these explanations are directly associated with VO_4^{3-} groups (ions, while $Ag_4V_2O_7$ is a crystalline solid composed of a structural framework formed by interconnected ($[VO_4]$–$[AgO_5]$–$[VO_4]$–$[AgO_6]$...) clusters (see Fig. 2(b)). Therefore, we can assume that the distorted tetrahedral $[VO_4]$ clusters and distorted trigonal bipyramidal $[VO_5]$ clusters are the main responsible through electronic transitions between the VB and CB.

As there is an interconnection between the distorted trigonal bipyramidal $[AgO_5]$ clusters and the distorted octahedral $[AgO_6]$ clusters in the orthorhombic lattice, it is possible to conclude that any distortion caused on the $[VO_4]$ and $[VO_5]$ clusters also promotes a slight deformation of the O–Ag–O bonds that form part of the chain. The association of different vanadium and silver clusters yields a wide range of polarization charges with the formation of electron–hole pairs between clusters. In instances involving electronic conduction properties, these clusters are able to present cluster-to-cluster charge transfer (CCCT) from vanadium to silver (or vice-versa) by means of excitations involving electronic transitions. This CCCT mechanism induces the formation of different energy levels within the forbidden band gap (structural order–disorder effect). Particularly, this phenomenon has its origin during the crystal formation and organization stages, which are directly dependent on interactions between tetrahedral/trigonal bipyramidal $[VO_z]$ (z= 4 and 5) clusters and trigonal bipyramidal/octahedral $[AgO_y]$ (y= 6 and 5) clusters. Therefore, these structural defects promote a symmetry break, causing polarization of the structure by electronic charge transfer from ordered (o) to disordered (d) clusters (formation of electron–hole pairs). The corresponding equations are presented in Support Information, S4.

The PL bands arise from photogenerated electron–hole pair processes and the electronic transition between the VB (2*p* levels of O atoms and 4*d* levels of Ag atoms) and the CB (3*d* levels of V atoms). Breaking symmetry processes in these clusters with distortions and tilts create a huge number of different structures and subsequently different material properties related to local (short), intermediate, and long-range structural order–disorder.

4. Conclusions

In summary, new research on the synthesis of $Ag_4V_2O_7$ crystals with novel properties has attracted great attention because of the variety of their potential applications. This study not only provides new information on the geometry, cluster coordination, and electronic structure of $Ag_4V_2O_7$ microcrystals, but also illustrates the potential of combining experimental techniques and first-principles DFT calculations. This combination led us to develop a systematic procedure to study the structure and electronic DOS of $Ag_4V_2O_7$. We found that it exhibits an orthorhombic structure, formed by two types of clusters of V atoms, $[VO_4]$ and $[VO_5]$, and two types of clusters of Ag atoms, $[AgO_5]$ and $[AgO_6]$. These clusters act as building blocks for the $Ag_4V_2O_7$ structure. Features in the Raman spectra were identified through comparison with calculated vibrational frequencies, and this confirmed the predicted structure of this material. The UV-vis spectrum indicated that $Ag_4V_2O_7$microcrystals have a direct band gap with a value of E_{gap}= 2.45 eV. The present work provides a new direction toward the design of this crystalline material and the search for practical applications in, for example, biology, catalysis, and photoluminescent materials. This knowledge may help in developing effective processing routines to enhance the performance of bulk heterojunction solar cells. With the combined insight provided by multiscale simulations and experiments, it may be possible to develop effective tempering routes to fine-tune the electronic structure of organic semiconductor materials. This would allow developing nanostructure arrays with great potential in technological applications such as optical sensors and photoelectronic materials.

Acknowledgements

The authors acknowledge the financial support of agencies: CAPES (PNPD – 1268069), FAPESP (2013/07296-2; 2013/26671- 9), CNPq (304531/2013-8), Generalitat Valenciana for PrometeoII/2014/022 and ACOMP/2014/270, Ministerio de Economia y Competitividad, project CTQ2012-36253-C03-02, and to the Spanish Brazilian program (PHBP14-00020). We also acknowledge the Servei Informática, Universitat Jaume I for a generous allotment of computer time. J.A. acknowledges to Ministerio de Economia y Competitividad, "Salvador Madariaga" program, PRX15/00261. L.G. acknowledges Banco Santander (Becas Iberoamérica: Jóvenes profesores e investigadores).

References

1. K. J. Takeuchi, A. C. Marschilok, S. M. Davis, R. A. Leising and E. S. Takeuchi, *Coordination Chemistry Reviews*, 2001, **219**, 283.
2. R. Konta, H. Kato, H. Kobayashi and A. Kudo, *Physical Chemistry Chemical Physics*, 2003, **5**, 3061.
3. J. Ren, W. Wang, M. Shang, S. Sun, L. Zhang and J. Chang, *Journal of Hazardous Materials*, 2010, **183**, 950.
4. X. Hu, C. Hu and J. Qu, *Materials Research Bulletin*, 2008, **43**, 2986.
5. C. M. Huang, G. T. Pan, Y. C. M. Li, M. H. Li and T. C. K. Yang, *Applied Catalysis a-General*, 2009, **358**, 164.
6. C. M. Huang, K. W. Cheng, G. T. Pan, W. S. Chang and T. C. K. Yang, *Chemical Engineering Science*, 2010, **65**, 148-152.
7. L. C. Chen, G. T. Pan, T. C. K. Yang, T. W. Chung and C. M. Huang, *Journal of Hazardous Materials*, 2010, **178**, 644.

8. Z. Chen, S. Gao, R. Li, M. Wei, K. Wei and H. Zhou, *Electrochimica Acta*, 2008, **53**, 8134.
9. J. Wang, X. Yang, J. Chen, J. Xian, S. Meng, Y. Zheng, Y. Shao and D. Li, *Journal of the American Ceramic Society*, 2014, **97**, 267.
10. J. Wang, J. Chen, Y. Yu, W. Yu, X. Meng, J. Chen and D. Li, *Crystengcomm*, 2015, **17**, 6661.
11. L. Mai, L. Xu, Q. Gao, C. Han, B. Hu and Y. Pi, *Nano Letters*, 2010, **10**, 2604.
12. W. D. Chemelewski, O. Mabayoje and C. B. Mullins, *Journal of Physical Chemistry C*, 2015, **119**, 26803.
13. L. Liang, Y. Xu, Y. Lei and H. Liu, *Nanoscale*, 2014, **6**, 3536.
14. S. Liang, J. Zhou, X. Zhang, Y. Tang, G. Fang, T. Chen and X. Tan, *Crystengcomm*, 2013, **15**, 9869.
15. L. Liang, H. Liu and W. Yang, *Nanoscale*, 2013, **5**, 1026.
16. Y. Sang, L. Kuai, C. Chen, Z. Fang and B. Geng, *Acs Applied Materials & Interfaces*, 2014, **6**, 5061.
17. Q. Zhu, W. S. Wang, L. Lin, G. Q. Gao, H. L. Guo, H. Du and A.-W. Xu, *Journal of Physical Chemistry C*, 2013, **117**, 5894.
18. M. R. Parida, C. Vijayan, C. S. Rout, C. S. S. Sandeep and R. Philip, *Applied Physics Letters*, 2012, **100**, 1211191.
19. P. Ju, H. Fan, B. Zhang, K. Shang, T. Liu, S. Ai and D. Zhang, *Separation and Purification Technology*, 2013, **109**, 107.
20. H. Xu, H. Li, L. Xu, C. Wu, G. Sun, Y. Xu and J. Chu, *Industrial & Engineering Chemistry Research*, 2009, **48**, 10771.
21. H. Shi, Z. Li, J. Kou, J. Ye and Z. Zou, *Journal of Physical Chemistry C*, 2011, **115**, 145.
22. S. Kittaka, S. Nishida and T. Ohtani, *Journal of Solid State Chemistry*, 2002, **169**, 139.
23. R. Masse, M. T. Averbuchpouchot, A. Durif and J. C. Guitel, *Acta Crystallographica Section C-Crystal Structure Communications*, 1983, **39**, 1608.
24. T. A. Albrecht, C. L. Stern and K. R. Poeppelmeier, *Inorganic Chemistry*, 2007, **46**, 1704.
25. R. Ran, J. G. McEvoy and Z. Zhang, *Materials Research Bulletin*, 2016, **74**, 140.
26. C. Belver, C. Adan, S. Garcia-Rodriguez and M. Fernandez-Garcia, *Chemical Engineering Journal*, 2013, **224**, 24.
27. V. M. Longo, C. C. De Foggi, M. M. Ferrer, A. F. Gouveia, R. S. Andre, W. Avansi, C. E. Vergani, A. L. Machado, J. Andres, L. S. Cavalcante, A. C. Hernandes and E. Longo, *Journal of Physical Chemistry A*, 2014, **118**, 5769.
28. P. S. Lemos, A. Altomare, A. F. Gouveia, I. C. Nogueira, L. Gracia, R. Llusar, J. Andres, E. Longo and L. S. Cavalcante, *Dalton Transactions*, 2016, **45**, 1185.
29. Y. V. B. De Santana, J. E. Cardoso Gomes, L. Matos, G. H. Cruvinel, A. Perrin, C. Perrin, J. Andres, J. A. Varela and E. Longo, *Nanomaterials and Nanotechnology*, 2014, **4**, DOI: 10.5772/58923.
30. E. Longo, D. P. Volanti, V. M. Longo, L. Gracia, I. C. Nogueira, M. A. P. Almeida, A. N. Pinheiro, M. M. Ferrer, L. S. Cavalcante and J. Andres, *Journal of Physical Chemistry C*, 2014, **118**, 1229.
31. L. F. da Silva, A. C. Catto, W. Avansi, Jr., L. S. Cavalcante, J. Andres, K. Aguir, V. R. Mastelaro and E. Longo, *Nanoscale*, 2014, **6**, 4058.
32. R. A. Roca, J. C. Sczancoski, I. C. Nogueira, M. T. Fabbro, H. C. Alves, L. Gracia, L. P. S. Santos, C. P. De Sousa, J. Andrés, G. E. Luz, E. Longo and L. S. Cavalcante, *Catalysis Science & Technology*, 2015, **5**, 4091.
33. M. T. Fabbro, C. Saliby, L. R. Rios, F. A. La Porta, L. Gracia, M. S. Li, J. Andres, L. P. S. Santos and E. Longo, *Science and Technology of Advanced Materials*, 2015, **16**, 65002.
34. G. Botelho, J. C. Sczancoski, J. Andres, L. Gracia and E. Longo, *Journal of Physical Chemistry C,* 2015, **119**, 6293.
35. G. Botelho, J. Andres, L. Gracia, L. S. Matos and E. Longo, *ChemPhysChem*, 2015, **81**, 202.
36. R. Dovesi, V. R. Saunders, C. Roetti, R. Orlando, C. M. Zicovich-Wilson, F. Pascale, B. Civalleri, K. Doll, N. M. Harrison, I. J. Bush, P. D'Arco, M. Llunell, C. M. and N. Y., *Crystal14 User's Manual*, University of Torino, Torino, 2014.
37. F. Cora, A. Patel, N. M. Harrison, R. Dovesi and C. R. A. Catlow, *Journal of the American Chemical Society*, 1996, **118**, 12174.
38. CRYSTAL - Basis Sets Library, http://www.crystal.unito.it/basis-sets.php, (accessed March, 2016).
39. S. Grimme, *Journal of Computational Chemistry*, 2006, **27**, 1787.
40. T. Bucko, J. Hafner, S. Lebegue and J. G. Angyan, *Journal of Physical Chemistry A*, 2010, **114**, 11814.
41. G. Kresse and J. Hafner, *Physical Review B*, 1994, **49**, 14251.
42. M. Marsman, J. Paier, A. Stroppa and G. Kresse, *Journal of Physics-Condensed Matter*, 2008, **20**, 642011.
43. H. M. Rietveld, *Journal of Applied Crystallography*, 1969, **2**, 65.
44. H. M. Rietveld, *Acta Crystallographica*, 1967, **22**, 151.
45. A.C. Larson and R. B. V. Dreele, *Los Alamos: National Laboratory*, 2001, 124.
46. K. Momma and F. Izumi, *Journal of Applied Crystallography*, 2011, **44**, 1272.
47. K. Momma and F. Izumi, *Journal of Applied Crystallography*, 2008, **41**, 653.
48. L. S. Cavalcante, M. A. P. Almeida, W. Avansi, Jr., R. L. Tranquilin, E. Longo, N. C. Batista, V. R. Mastelaro and M. Siu Li, *Inorganic Chemistry*, 2012, **51**, 10675.
49. D. L. Rousseau, R. P. Bauman and S. P. S. Porto, *Journal of Raman Spectroscopy*, 1981, **10**, 253.
50. D. G. Stroppa, L. A. Montoro, A. Campello, L. Gracia, A. Beltran, J. Andres, E. R. Leite and A. J. Ramirez, *Physical Chemistry Chemical Physics*, 2014, **16**, 1089.
51. M. R. D. Bomio, R. L. Tranquilin, F. V. Motta, C. A. Paskocimas, R. M. Nascimento, L. Gracia, J. Andres and E. Longo, *Journal of Physical Chemistry C*, 2013, **117**, 21382.
52. V. M. Longo, L. Gracia, D. G. Stroppa, L. S. Cavalcante, M. Orlandi, A. J. Ramirez, E. R. Leite, J. Andres, A. Beltran, J. A. Varela and E. Longo, *Journal of Physical Chemistry C*, 2011, **115**, 20113.
53. J. Andres, L. Gracia, A. F. Gouveia, M. M. Ferrer and E. Longo, *Nanotechnology*, 2015, **26**, 405703.
54. M. Ferrer, A. Gouveia, L. Gracia, E. Longo and J. Andrés, *Modelling and Simulation in Materials Science and Engineering*, 2016, **24**, 25007.
55. D. Koziej, A. Lauria and M. Niederberger, *Advanced Materials*, 2014, **26**, 235.
56. M. V. Kovalenko, L. Manna, A. Cabot, Z. Hens, D. V. Talapin, C. R. Kagan, V. I. Klimov, A. L. Rogach, P. Reiss, D. J. Milliron, P. Guyot-Sionnnest, G. Konstantatos, W. J. Parak, T. Hyeon, B. A. Korgel, C. B. Murray and W. Heiss, *ACS Nano*, 2015, **9**, 1012.

57. J. F. Nye, *Physical Properties of Crystals: Their Representation by Tensors and Matrices*, Oxford University Press , Oxford, 1985.
58. T. Vehoff, B. Baumeier, A. Troisi and D. Andrienko, *Journal of the American Chemical Society*, 2010, **132**, 11702.
59. T. Vehoff, Y. S. Chung, K. Johnston, A. Troisi, D. Y. Yoon and D. Andrienko, *Journal of Physical Chemistry C*, 2010, **114**, 10592.
60. M. Mas-Torrent, P. Hadley, S. T. Bromley, X. Ribas, J. Tarres, M. Mas, E. Molins, J. Veciana and C. Rovira, *Journal of the American Chemical Society*, 2004, **126**, 8546.
61. A. B. Cairns and A. L. Goodwin, *Chemical Society Reviews*, 2013, **42**, 4881.
62. Y. Pu, Y. Huang, T. Tsuboi, H. Cheng and H. J. Seo, *Rsc Advances*, 2015, **5**, 73467.
63. A. D. J. David, G. S. Muhammad and V. Sivakumar, *International Journal of Luminescence and applications*, 2015, **5**, 393.